Title Page

Name of the authors: Greg Chipman, Bryant Johnson, Cameron Vann, Lance Whitesides, Devin Rappleye

Title: Experimental Determination of the Electrochemical Properties of Bismuth Chloride in Eutectic LiCl-KCl and LiCl-KCl-$CaCl_2$ Molten Salts

Affiliation and address of the authors: Department of Chemical Engineering, Brigham Young University, Provo, UT 84602, USA

Email address of the corresponding author: chipm@byu.edu

Declaration of interests

☒ The authors declare that they have no known competing financial interests or personal relationships that could have appeared to influence the work reported in this paper.

☐ The authors declare the following financial interests/personal relationships which may be considered as potential competing interests:

The authors declare that the data supporting the findings of this study are available within the paper. Should any raw data files be needed in another format they are available from the corresponding author upon reasonable request.

This version of the article has been accepted for publication, after peer review and is subject to Springer Nature's AM terms of use, but is not the Version of Record and does not reflect post-acceptance improvements, or any corrections. The Version of Record is available online at:

Chipman, G., Johnson, B., Vann, C., Whitesides, L., & Rappleye, D. (2024). Experimental determination of the electrochemical properties of bismuth chloride in eutectic LiCl–KCl and LiCl–KCl–CaCl2 molten salts. *Journal of Radioanalytical and Nuclear Chemistry*. https://doi.org/10.1007/s10967-024-09354-4

Experimental Determination of the Electrochemical Properties of Bismuth Chloride in Eutectic LiCl-KCl and LiCl-KCl-$CaCl_2$ Molten Salts

Greg Chipman[a,*], Bryant Johnson[a], Cameron Vann[a], Lance Whitesides[a], Devin Rappleye[a]

[a]Department of Chemical Engineering, Brigham Young University, Provo, UT 84602, USA

Abstract

Bismuth has been investigated as a potential liquid electrode for molten salt electrorefining, but the electrochemical behavior of Bi^{3+}/Bi redox couple has received scant attention in LiCl-KCl and LiCl-KCl-$CaCl_2$ eutectics. Electroanalytical techniques were used to determine properties of Bi^{3+}/Bi. Diffusivities of 6.71 and 8.93 x 10^{-6} cm^2 s^{-1} and standard apparent potentials of 0.1166 and 0.1187 V vs. Ag/AgCl (4.75 mol%) were recommended for $BiCl_3$ in LiCl-KCl and LiCl-KCl-$CaCl_2$ eutectics, respectively, at 680±3.1 K. The ICP-MS analysis of $BiCl_3$ content limited the accuracy of the results. The reliability of the results improved with a more thorough drying procedure for $CaCl_2$.

Keywords

Bismuth Chloride, Molten Salt, Cyclic Voltammetry, Liquid Metal, Electrorefining, Pyroprocessing

1. Introduction

Electrochemical properties are important to be able to model and understand the physical behavior occurring during processes such as electrorefining and electrowinning. The electrochemical properties for bismuth have yet to be determined in the LiCl-KCl-$CaCl_2$ eutectics and only limited results exist in the LiCl-KCl eutectic [1, 2]. The electrochemical properties of bismuth are of interest because it has recently been identified as a possible surrogate for plutonium electrorefining [3]. Bismuth is also being developed as a liquid cathode for the electrorefining of used nuclear fuel [4, 5]. One common issue with the use of liquid cathodes is dendrite formation on the molten cathode [6–11]. Understanding the electrochemical properties of these liquid cathodes, such as bismuth, will assist in mitigating these and other challenges currently faced in these operations. The LiCl-KCl-$CaCl_2$ eutectics are also of interest because they offer advantages such as lower melting points (see Figure 1) and higher oxide solubilities [12]. Although the latter benefit has been questioned by Vishnu et al. [13] and may be offset by more sluggish kinetics at lower temperatures. The determination of the electrochemical properties and behavior of bismuth in the LiCl-KCl-$CaCl_2$ (LiCl:KCl:$CaCl_2$ = 50.5:44.2:5.3mol%) and LiCl-KCl eutectics will help elucidate tradeoffs and potential improvements for processes in which bismuth is used.

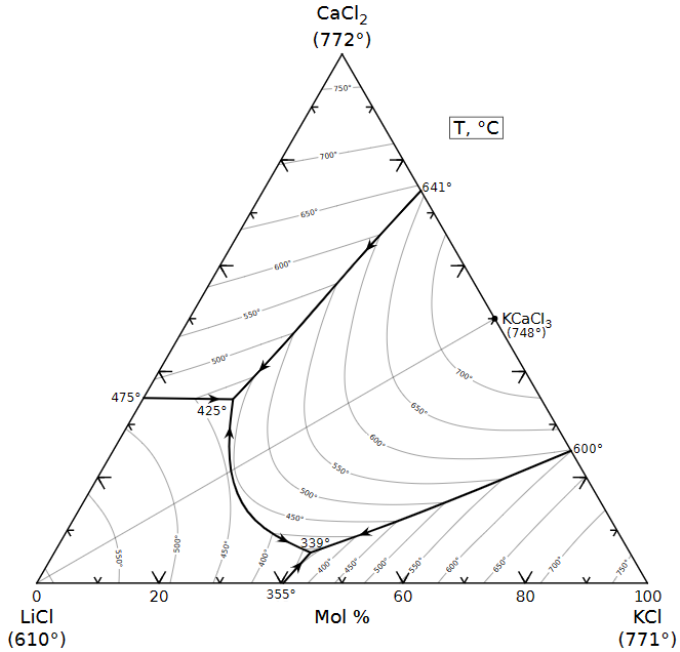

Fig. 1 Liquidus projection of the KCl-LiCl-$CaCl_2$ system, reproduced from [14]

While the electrochemical properties of bismuth have not been determined in the LiCl-KCl-$CaCl_2$ eutectics, there have been some electrochemical studies of bismuth in other molten salts [15–18]. The electrochemical behavior of bismuth in the LiCl-KCl eutectic has previously been investigated using cyclic voltammetry to identify the oxidation and reduction peaks present [19]. The standard redox potential, diffusivity, standard rate constant, and exchange current density of the bismuth electrodeposition reaction were determined using cyclic voltammetry, chronopotentiometry, and chronoamperometry in the $PbCl_2$-KCl eutectic [20]. The standard redox potential of the bismuth electrodeposition reaction and the diffusivity of bismuth in the LiCl-KCl eutectic were reported by Plambeck et. al. [1] and Carlin et. al. [2], respectively. Laitinen and colleagues also published some studies involving bismuth chloride [21, 22]. To the knowledge of the authors, no other work exists that measures the electrochemical parameters of the bismuth chloride to bismuth metal reduction in molten salts. In this work, the standard redox potential, number of electrons exchanged, and diffusivity of bismuth ions in the bismuth electrodeposition reaction will be determined using cyclic voltammetry (CV), square wave voltammetry (SWV), chronoamperometry (CA), chronopotentiometry (CP), and open-circuit potential (OCP) measurements in the LiCl-KCl and LiCl-KCl-$CaCl_2$ eutectics.

2. Experimental

2.1 Electrochemical Cell

The electrochemical experiments were conducted in an inert atmosphere argon glovebox (< 10 ppm O_2/H_2O). Alumina crucibles (Advalue Tech, AL-2100) were used to contain the molten salt and were heated inside of an MTI tube furnace (OTF-1200X-S-NT). In each run, the alumina crucible was placed atop two inverted alumina crucibles to position it in the heating zone of the furnace. A nickel tube was placed around the alumina crucibles to center the crucibles and to provide a Faraday cage for the electrochemical experiments. A schematic and picture of the

experimental set-up are shown in Figure 2. Electrochemical experiments were conducted using an Autolab potentiostat (PGSTAT302N) controlled by NOVA 2.1 software. The electrodes were connected to the potentiostat using binding posts on the wall of the glovebox. More details about this experimental setup can be found elsewhere [23, 24].

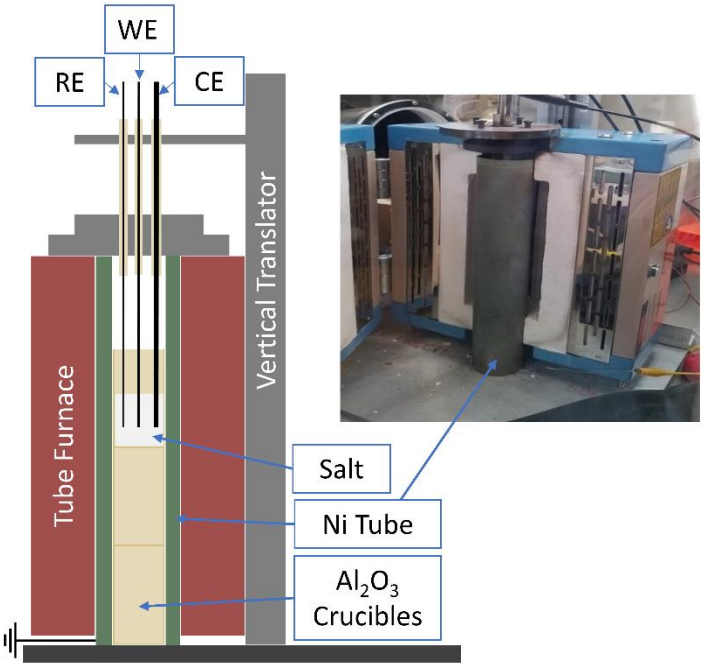

Fig. 2 Experimental set-up used for the $BiCl_3$ electrochemical experiments

The bismuth (III) chloride (Ultra Dry, 99.997+% metals basis, Thermo Scientific Chemicals, 035680.06) was used as received and was added to the crucible with eutectic mixtures of LiCl-KCl (59.2:40.8 mol%) or LiCl-KCl-$CaCl_2$ (50.5:44.2:5.3 mol%) prior to melting the salts for the experiments. In each run, the $BiCl_3$ was added to the eutectic salt to target a concentration of at least 0.3 mol% (8.4×10^{-5} mol cm^{-3}) $BiCl_3$. LiCl (>99%, Alfa Aesar, 36217), KCl (>99%, Alfa Aesar, 11595), and $CaCl_2 \cdot 2H_2O$ (>99%, Alfa Aesar, 33296) were dried in an oven (Across International, AT32e) under vacuum following the procedures shown in Table 1. The procedures in Table 1 are based on thermogravimetric analysis, titrations, and weight loss measurements published elsewhere [25–27]. After each salt was dried, a salt block of eutectic LiCl-KCl-$CaCl_2$ was made by placing the appropriate amounts of calcium chloride, lithium chloride, and potassium chloride in a large alumina crucible in a furnace, which was heated to 1023 K. The furnace was held at that temperature for three hours to allow for the eutectic salt to form. After three hours, the furnace was cooled, and the eutectic salt block was removed from the alumina crucible. Portions of the obtained eutectic salt block were used for runs 2 and 3. The LiCl-KCl eutectic was made in an alumina crucible (electrolyte for runs 1 and 5), a mullite tube (reference electrode solution for runs 1 and 4), and pyrex tube (reference electrode solution for runs 5 and 6) by heating the appropriate amounts of LiCl-KCl to 973 K in the MTI tube furnace for two hours to allow the salts to fuse in their respective containers. For runs 4 and 6, $CaCl_2$, KCl, and $BiCl_3$ were added to the LiCl-KCl eutectic from runs 1 and 5 respectively to form the LiCl-KCl-$CaCl_2$ eutectic and maintain the same target mol% $BiCl_3$ as in the LiCl-KCl eutectic. Six experimental runs were performed with the details of each run summarized in Table 2.

Table 1 Vacuum drying steps used for reducing moisture in the LiCl, KCl, and $CaCl_2$ salts

Steps	LiCl/KCl		$CaCl_2$ (Runs 2 and 3)		$CaCl_2$ (Runs 4 and 6)	
	T / K	Time / hrs	T / K	Time / hrs	T / K	Time / hrs
1	298	8	373	8	298	5
2	383	8	388	8	363	11
3	459	8	522	60	393	8
4	522	24	---	---	503	48

Table 2 Experimental details for the bismuth chloride electrochemical experiments

Run	$BiCl_3$ Weighed /g	Eutectic Salt System	Eutectic Salt /g	$BiCl_3$ ICP-MS Concentration /10^{-5} mol cm^{-3}	Temperature /K	WE Surface Area /cm^2
1[a,b]	1.05	LiCl-KCl	60.6	7.18 ± 0.895	681 ± 1.1	0.670 ± 0.0014
2[b]	1.57	LiCl-KCl-$CaCl_2$	60.0	4.24 ± 0.449	681 ± 1.1	1.374 ± 0.0006
3[b]	1.57	LiCl-KCl-$CaCl_2$	60.0	4.24 ± 0.449	686 ± 1.1	0.766 ± 0.0006
4[a,b]	1.34	LiCl-KCl-$CaCl_2$	77.5	7.75 ± 0.966	678 ± 1.1	0.748 ± 0.0073
5[c]	1.78	LiCl-KCl	54.7	10.4 ± 1.92	681 ± 1.1	0.786 ± 0.0013
6[c]	2.02	LiCl-KCl-$CaCl_2$	70.9	9.92 ± 1.84	679 ± 1.1	1.263 ± 0.0020

[a]Ag/AgCl RE with mullite membrane, [b]W qRE, [c]Ag/AgCl RE with pyrex membrane

Three reference electrodes were used in the electrochemical experiments. Two different REs were used to conduct the OCP measurements. For runs 1 and 4, a solution of 4.5 mol% AgCl (99.997% metals basis, Alfa Aesar, 10857) in the LiCl-KCl eutectic was formed inside of a one-end closed mullite tube (OD 11.13 mm, McDanel Advanced Ceramic Technologies, MV0160431-06-12). A 0.64 mm diameter Ag wire (99.9% metals basis, Alfa Aesar, 43325) was used as the contact in the reference solution and the electrical lead for the reference electrode (RE) to measure the OCP. The wall of the mullite tube was 1.59 mm thick and was thinned approximately to half the original thickness near the closed end to the tube using a tile saw. For runs 5 and 6, a solution of 4.75 mol% AgCl in the LiCl-KCl eutectic was formed inside of a thin-walled (0.55 mm thick), one-end-closed pyrex tube (OD 10 mm, Wilmad Glass Company, 513-1PP). Another 0.64 mm Ag wire was used to provide electrical contact with the reference solution to measure the OCP. The thin-walled pyrex tube was used to reduce the membrane potential [28, 29]. Hence, runs 5 and 6 were used for making more accurate OCP measurements.

A 1.5 mm diameter tungsten rod (99.95% metals basis, Thermo Scientific, 042233.CE) was used as a quasi-reference electrode (qRE) for the CV, CA, SWV, and CP measurements conducted. The working electrode (WE) for all experiments was a 1.5 mm diameter tungsten rod (99.95% metals basis, Thermo Scientific, 042233.CE) with the counter electrode (CE) being a 3.175 mm diameter tungsten rod (99.95% metals basis, Thermo Scientific, 010407.BY). The WE, CE, and qRE were sheathed using alumina tubes above the molten salt. The electrodes were aligned using a custom lid and attachment to the vertical translator. The WE was raised and lowered using a vertical translator. The WE surface area was determined by adjusting the depth of the WE using the vertical translator (Velmex, A2509P10-S2.5-TL, 0.0254 mm precision) in precise increments and conducting CV measurements after each adjustment. Using the relationship between the peak

height and the change in area, the WE surface area could be calculated for the electrochemical experiments (see Section 3.1).

2.2. Electrochemical Techniques

Electrochemical measurements were conducted in a manner where the results were verified to be reproducible. At least two runs of each measurement were conducted at the same conditions using a randomized order. The WE was anodically cleaned between each experiment using a CV procedure with 15 scans between 0.3 V and 0.7 V vs. the qRE. When the current in the CV scans began to not change from scan to scan it was validated that the WE had been sufficiently cleaned. After the WE was cleaned, a 90 second rest time was used to allow time for the system to relax before the start of each experiment.

CV measurements were conducted using scan rates between 0.025 and 1 V s^{-1} and a digital staircase step of -1 mV (initially, 1 mV after scan reversal). 4 scans were performed to verify repeatability. The 3rd scan was used for any analysis, if identical to the 2nd and 4th scan. SWV experiments were conducted in a frequency range from 1-50 Hz. The step size was -2 mV and the amplitude of the square wave was 0.05 V. CA experiments were conducted by applying 1 V vs. the qRE for 20 seconds and then applying between -0.05 and -0.25 V vs. the qRE for 1 second. CP experiments were conducted by allowing the cell to rest at 0 A for 5-20 seconds, after which a current between -0.005 and -0.1 A was applied for sufficient time to reach a potential below -0.2 V. OCP measurements were conducted directly after some of the CP measurements by allowing the system to relax for 300 s while recording the WE potential. All electrochemical measurements were compensated for ohmic (IR) drop through a positive feedback loop on the potentiostat at a level between 75-85% of the IR resistance determined by electrochemical impedance spectroscopy (EIS) except for the CP and OCP measurements. CP measurements were corrected for the IR resistance after the measurements were completed. The OCP measurements do not require IR compensation as no current is applied during the measurement.

2.3 Chemical Analysis

Three samples were collected from each run for compositional analysis using inductively coupled plasma mass spectroscopy (ICP-MS, Agilent 7900). Portions of each sample were weighed before being dissolved in 20% HNO_3/HCl (5:1) solution and diluted to 2% HNO_3/HCl. The bismuth content of each solution was measured with ICP-MS. Standard addition was used to minimize the known matrix effects of bismuth with lithium and calcium. Matrix effects occur when the presences of an species suppress or enhance the signal of another species [30]. "Significant matrix effects of Bi in the ICP-MS require the use of matrix matched standard solutions for calibration" [31]. The standard addition method reduces error by matrix matched standard solutions [32]. The ICP-MS measurements were used to determine the weight fraction of bismuth in the sample. The reported weight percents from runs 1 and 5 were converted to concentrations using a density value for the LiCl-KCl eutectic of 1.669 ± 0.0100 g cm^{-3} taken from the literature [33]. The reported weight percents from runs 2-4 and 6 were converted to concentrations using a density value for the LiCl-KCl-$CaCl_2$ eutectic of 1.713 ± 0.0103 g cm^{-3}. The density value for the LiCl-KCl-$CaCl_2$ eutectic was calculated using the solid density value for $CaCl_2$ and assuming ideal mixing of eutectic LiCl-KCl and $CaCl_2$. Experimental data reported in the literature shows that LiCl, KCl,

and $CaCl_2$ all approximate ideal behavior in their binary systems [34, 35] indicating that ideal mixing likely introduces minimal error. Density errors were estimated to be ±0.60% by assuming the maximum reported error (0.36%) for Janz's regression of density data for LiCl-KCl system [35] plus an additional 0.22% to estimate the error in the density for unaccounted perturbations from the eutectic compositions, as great as 1 wt.%. Density errors were included when calculating the error (95% confidence interval) of the ICP-MS measured concentration of bismuth from the results from all 3 samples for each run.

3. Results and Discussion

3.1 WE Area Determination

The determination of the WE surface area is key as it is used to calculate the diffusivity. The uncertainty in the area measurement propagates into the uncertainty for the diffusivity measurement. While visual methods were tried initially, these methods have uncertainties on the order of 10% [36]. CV measurements can be used to determine the WE surface area by taking advantage of the linear relationship between WE surface area and peak height. This relationship is described by the Berzins-Delahay equation shown in Eq. (1):

$$I_p = 0.6105A\sqrt{\frac{(nF)^3 D_o \upsilon}{RT}}C_o^* \quad (1)$$

where I_p represents the peak current, A is the WE surface area, n is the number of electrons exchanged, F is Faraday's constant, D_o is the diffusivity of the oxidized species, ν is the scan rate, R is the ideal gas constant, T is the temperature, and C_o^* is the bulk concentration of the oxidized species. To determine the area, CV measurements using the same conditions were taken at known height differences using the vertical translator to raise or lower the WE a known amount. The relationship between the WE surface area and peak height was then determined by shifting the y-intercept to zero as a WE surface area of zero should correspond with a peak current height of zero. An example of the initial measurements taken and of the shifted data are shown in Figure 3 for the area determination of run 2. The equation shown on the graph showing the adjusted data can be used to determine the WE surface area from the peak height of a cyclic voltammogram conducted at the same conditions. Using the standard error from 'LINEST' function from Microsoft© Excel, the 95% confidence interval (CI) was calculated to be < 1% of the determined area (see Table 2). The same method was used to determine the WE surface area for each of the runs.

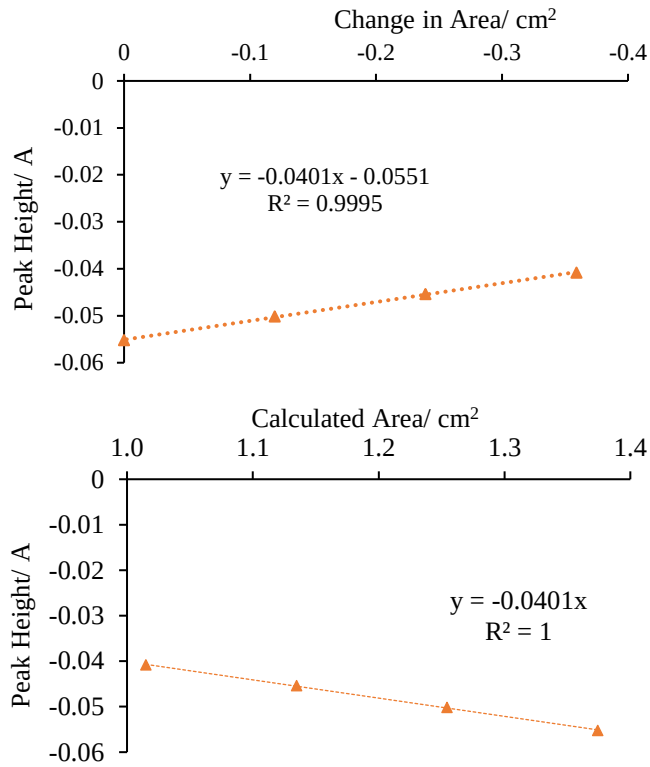

Fig. 3 CV peak heights for Bi electrodeposition in molten LiCl-KCl-$CaCl_2$ eutectic to determine WE surface area from run 2. Top: Raw data of peak height vs. depth (area) adjustment, Bottom: Adjusted data to make the linear fit pass through the origin. WE: 1.5 mm W rod, qRE: 1.5 mm W rod, CE: 3.175 mm W rod, 80% IR compensation, CV upper limit: 0.4 V, CV lower limit: -0.1 V, Scan Rate: 0.1 V s^{-1}

3.2 Full Electrochemical Window Scans

Initial orientation to the electrochemical system was accomplished by determining the full electrochemical window (FEW) and identifying the observed peaks. In each run, a cyclic voltammogram was run to determine the upper and lower limit of the electrochemical window. FEWs from runs 1, 2 and 4 are shown in Figure 4 with the FEW from run 1 being shifted by 0.06 V to align the A/A' signals with the FEWs of other runs. A list of the half-cell reactions attributed to the signals identified in the FEWs is given in Table 3. The attributions of half-cell reactions are based on previous studies in the literature as detailed in the following discussion.

Table 3 List of reactions attributed to each signal in cyclic voltammograms.

Signal	Overall Redox Reaction
A/A'	$Cl_2 + 2e^- \leftrightarrow 2Cl^-$
B/B'	$Bi^{3+} + 3e^- \leftrightarrow Bi$
C/C'	$CaWO_4 + 6e^- \leftrightarrow W + Ca^{2+} + 4O^{2-}$
D/D'	$xCa^{2+} + 2e^- + yBi \leftrightarrow Ca_xBi_y$ and/or $xLi^+ + 1e^- + yBi \leftrightarrow Li_xBi_y$
E/E'	$Ca^{2+} + 2e^- \leftrightarrow Ca$ and/or $Li^+ + 1e^- \leftrightarrow Li$

First, the signals at the upper and lower limits of the FEW are discussed. The A/A' signals correspond to Cl_2/Cl^- redox couple—the upper limit of the window. The E/E' signals mark the lower limit of the window. In run 1, E/E' is the oxidation of Li and reduction of Li^+, respectively, as no calcium was present. In run 2 and 4, E is either the reduction of Ca^{2+} or the co-reduction of Ca^{2+} and Li^+ to a Ca-Li alloy and E' is the oxidation of the Ca-Li alloy based on previous studies [12, 13, 37]. In LiCl-KCl-$CaCl_2$ (52.3:11.6:36.1 mol%) eutectic, the reduction at the cathodic limit was found to be a lithium-calcium alloy based on ICP analysis of the cathode deposit [12]. In LiCl-KCl-$CaCl_2$ (50.5:44.2:5.3 mol%) eutectic [13] and LiCl-KCl eutectic containing $CaCl_2$ at more dilute concentrations [37], an additional reduction signal was visible at potentials slightly more positive than the sharp rise at the lower limit and was attributed to Ca^{2+} reduction. However, the additional signal was only visible at low scan rates (20 and 50 mV s^{-1}) and no chemical analysis of deposit on the W electrodes was presented to confirm the attribution. The Li^+ to Li reduction and oxidation signals (E/E') from run 1 are at a more negative potential than the E/E' signals from run 2. This would seem to indicate that the Ca^{2+} reduction or the Li^+ and Ca^{2+} co-reduction process occurs at a less negative potential than the Li^+ reduction process. However, the shift for E/E' is not observed in the bottom plot of Figure 4 for runs 1 (LiCl-KCl) and 4 (LiCl-KCl-$CaCl_2$). The drying procedure for $CaCl_2$ was improved for run 4. Hence, the shift of E/E' in run 2 is postulated to be due to more residual water being present in salt before melting, which led to increased hydrolysis of $CaCl_2$ during heating and more CaO or $Ca(OH)_2$ (i.e., O^{2-}, OH^-) in the molten salt [38, 39].

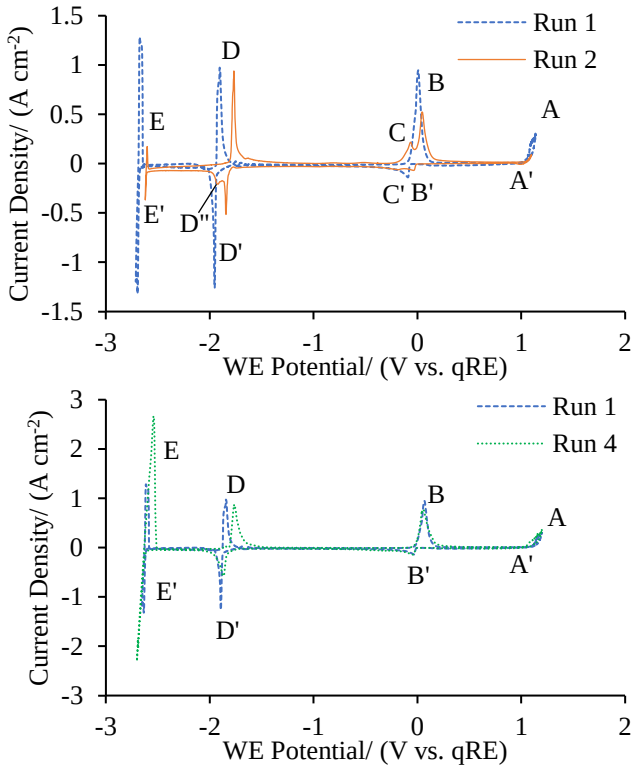

Fig. 4 Top: Full electrochemical window of $BiCl_3$ in molten LiCl-KCl eutectic (run 1) and LiCl-KCl-$CaCl_2$ eutectic (run 2). Bottom: Full electrochemical window of $BiCl_3$ in molten LiCl-KCl eutectic (run 1) and LiCl-KCl-$CaCl_2$ eutectic (run 4). WE: 1.5 mm W rod; qRE: 1.5 mm W rod; CE: 3.175 mm W rod; WE Area: 0.670 cm^2 (run 1), 1.374 cm^2 (run 2), 0.748 cm^2 (run 4); Scan Rate: 0.3 V s^{-1}; IR Compensation: 0.25 Ω/75% (run 1), 0.18 Ω/78% (run 2). 0.40 Ω/78% (run 4)

With the limits of the FEW and the associated signals identified, the peaks inside of the FEW, B/B', C/C', and D/D'/D" remained to be assigned. D' and D peaks are respectively attributed to the formation and oxidation of alloys of bismuth with lithium and calcium (when present). Peaks D and D' rise sharply and drop sharply back to the baseline current without a tail indicating that the reactions involve a reaction constrained by its availability on the surface of the WE (i.e., reaction of Li and/or Ca with thin Bi film on the surface of WE). In runs 2 and 4, the D and D' peaks commence at slightly more positive values in comparison to run 1. Hence, the formation of the Ca-Bi alloy may be slightly more favorable than the Li-Bi alloy. Two other papers have shown that the reduction potential of both lithium and calcium were shifted to less negative values in the presence of bismuth likely due to alloying [2, 40]. Peak C/C' and D" are unique to run 2 and hypothesized be related to increased presence of O^{2-} in the melt.

Peak B' is attributed to the single-step reduction of Bi^{3+} to bismuth metal. The relative position of the peak B's potential (~ 0 V) to the chlorine anion oxidation signal (~ 1 V) is similar to the difference of the standard redox potentials of Bi^{3+}/Bi and Cl^-/Cl_2 couples in the LiCl-KCl eutectic reported by Plambeck of -0.886 V [1]. Peak B is the oxidation of the deposited Bi metal. The standard redox potential of the Bi^{3+}/Bi in the LiCl-KCl-$CaCl_2$ eutectic and the LiCl-KCl eutectic are both determined in the OCP measurements reported hereafter (see Section 3.4). The C/C' peak couple is attributed to formation and reduction of calcium tungstate (W/$CaWO_4$), which involves the W electrode and CaO contamination. This reaction has been studied extensively in a previous publication [38] and is further confirmed in this publication by the absence of the C/C' peaks in CV measurements in LiCl-KCl eutectic and run 4, which used more carefully dried $CaCl_2$. This shows that the formation of $CaWO_4$ can be circumvented if the presence of moisture is assiduously avoided in the molten salts containing $CaCl_2$. Other electrodes were also considered for use to avoid $CaWO_4$ formation, but the only other options (Mo, Pt, Au, Ir, or Pd) also form side products (e.g., $CaMoO_4$) or alloy with bismuth [22, 41]. Therefore, the choice to run the experiments using a W electrode was made and the influence of the $CaWO_4$ peak was minimized.

3.3 Square Wave Voltammetry

SWV measurements were conducted to confirm the peak assignment of peak B' by calculating the number of electrons exchanged in the reaction associated with peak B' shown in Fig. 3. SWV profiles for some frequencies (*f*) from run 3 are shown in Figure 5 where the peak around 0 V vs. qRE is associated with the bismuth electrodeposition reaction and the peak around -0.2 V vs. qRE is associated with $CaWO_4$ reduction.

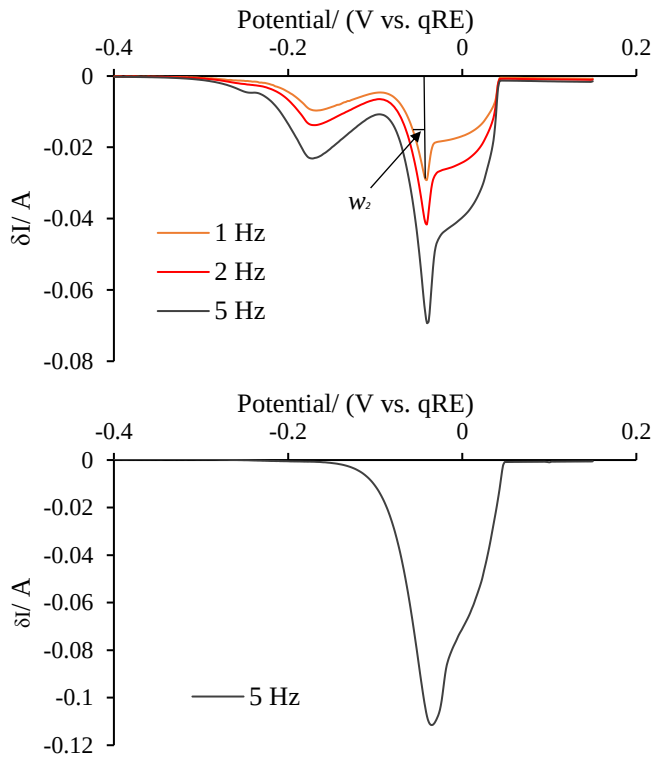

Fig. 5 Square wave voltammograms from run 3 (top) and run 4 (bottom). WE: 1.5 mm W rod; qRE: 1.5 mm W rod; CE: 3.175 mm W rod; WE Area: 0.766 cm^2 (run 3), 0.748 cm^2 (run 4); step potential: -0.002 V; amplitude: 0.05 V; IR Compensation: 0.25 Ω/85% (run 3), 0.40 Ω/78% (run 4).

Based on the work of Fatorous and Krulic [42], Fuller et al. developed a relation to determine the number of electrons exchanged for soluble-insoluble reactions with SWV data, which was used for the bismuth electrodeposition peak and is shown in Eq. (2) [43]:

$$w_2 = 0.91\frac{RT}{nF} \tag{2}$$

where w_2 is the width of the back half at half-maximum of the reduction peak (see Fig. 4) and the other variables are the same as defined previously. Eq. (2) assumes negligible uncompensated resistance and is applicable when w_2 is independent of frequency (f). The results determined for the number of electrons exchanged from each measurement are shown plotted against the square root pulse time (Δt) in Figure 6, where Δt = $1/(2f)$.

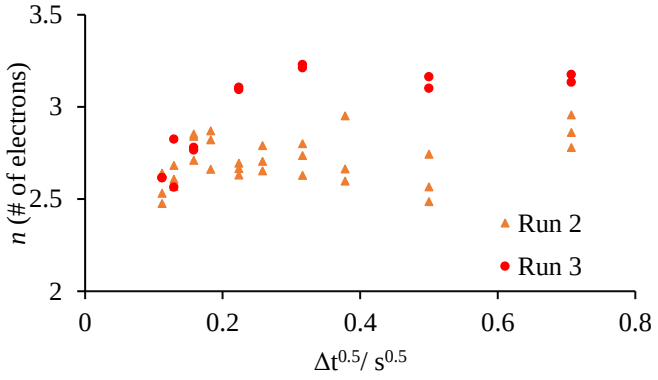

Fig. 6 Calculated n from SWV data for Bi^{3+} reduction peak. WE: 1.5 mm W rod; qRE: 1.5 mm W rod; CE: 3.175 mm W rod; WE Area: 1.374 cm^2 (run 2), 0.766 cm^2 (run 3); step potential: 0.002 V; amplitude: 0.05 V; IR compensation: 0.18 Ω/78% (run 2), 0.25 Ω/85% (run 3)

At the lower frequencies of 1-5 Hz ($\Delta t^{0.5}$ = 0.316 to 0.707 $s^{0.5}$), w_2 had no clear dependence on frequency, as portrayed in Eq. (2), and was used to calculate the *n* value for each of the runs. The average *n* values from runs 2 and 3 for the Bi^{3+} reduction peak were 2.7 ± 0.3 and 3.2 ± 0.1 respectively. These results confirm that peak B' corresponds to the three-electron exchange process of Bi^{3+} reduction. A thorough analysis of the $CaWO_4$ reduction peak can be found elsewhere [38], where the SWV peak needed to be deconvoluted due to a multi-step redox mechanism.

In run 4, SWV measurements had no evidence of $CaWO_4$ peak, as shown in bottom plot of Figure 5. Hence, the change in the $CaCl_2$ drying procedure (see Table 1) appears to be effective at reducing the interference from $CaWO_4$ peak to negligible levels. However, the higher resistance experienced in run 4 resulted in too significant of uncompensated resistance (0.113 Ω) to apply Eq. (2). Attempts were made to apply the more complicated relations developed by Fatorous and Krulic [42], which accounts for uncompensated resistance. However, this relation includes concentration of the analyte (i.e., $BiCl_3$), which introduced significant error (± >1) and could not be used to confidently confirm the number of electrons exchanged. Hence, runs 2 and 3 provide the most confident determination of the number of electrons exchanged because of the minimal number of variables involved in Eq. (2) and the lower uncompensated resistance.

3.4 Open Circuit Potential

OCP measurements were conducted to measure the standard redox potential of the bismuth electrodeposition reaction in both the LiCl-KCl and LiCl-KCl-$CaCl_2$ eutectics. A Ag/AgCl (4.5 mol%) RE was used for the OCP measurements for runs 1 and 4 while a Ag/AgCl (4.75 mol%) RE was used for runs 5 and 6. An example OCP measurement from run 4 is shown in Figure 7 where the cell is allowed to rest after applying a current for long enough to go below -1.5 V vs. the Ag/AgCl RE. The inset in the top plot of Figure 7 shows the initial transition from the bismuth alloy potential (see Fig. 3) to the Bi^{3+}/Bi potential.

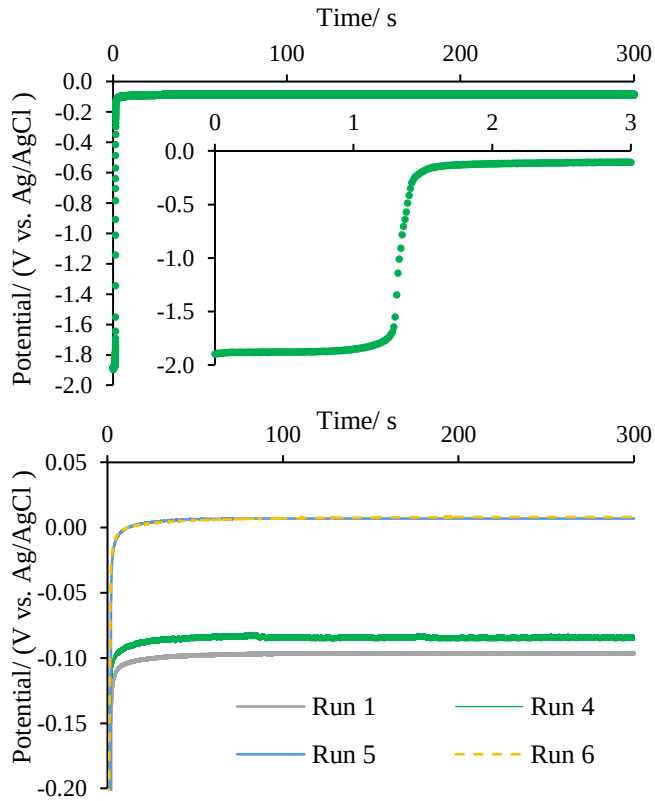

Fig. 7 Top: Example OCP measurement with inset of first 3 s from run 4 for $BiCl_3$ at 3.49×10^{-5} mol cm^{-3} in molten LiCl-KCl-$CaCl_2$ eutectic. WE: 1.5 mm W rod, RE: 4.5 mol% Ag/AgCl solution in a mullite tube, CE: 3.175 mm W rod. Bottom: Example OCP measurement from run 1, 4-6 for comparison. Experimental details for each run are shown in Table 3.

The OCP value for each measurement was calculated by taking the average recorded potential over the last 50 seconds. The OCP values from each measurement were then averaged to determine an average OCP value for each run. The Nernst equation, shown in Eq. (3), was used to calculate the standard apparent redox potential for the Bi^{3+}/Bi couple from the average OCP value.

$$E = E^{0'} - \frac{RT}{nF} ln\left(\frac{1}{x_{BiCl_3}}\right) \quad (3)$$

Where E is the OCP, $E^{0'}$ is the standard apparent redox potential, x_{BiCl_3} is the mole fraction of $BiCl_3$ and the other variables are the same as has been previously defined. The experimentally determined standard apparent redox potentials from the OCP measurements for runs 1 and 4-6 are shown in Table 4. The $E^{o'}$ value from run 1 (LiCl-KCl) is statistically different from the $E^{o'}$ value from run 4 (LiCl-KCl-$CaCl_2$). However, the difference is not significant between runs 5 and 6. Hence, the difference between runs 1 and 4 may be explained by the mullite membrane. The difference between $E^{o'}$ values using a mullite tube (runs 1 and 4) and a pyrex tube (runs 5 and 6) is significantly larger (0.09-0.1 V) than the difference between runs 1 and 4 (0.01 V) and runs 5 and 6 (0.001 V). The differences seen between different REs confirms that membranes can have a significant influence on the accuracy and repeatability of the observed OCP and resulting $E^{o'}$ calculated [29, 44]. Thus mullite tubes being larger and more variable in construction led to more significant and variable membrane potentials than the precision, thin-walled pyrex tubes [29].

Table 4 Standard redox potentials for bismuth electrodeposition in the LiCl-KCl (runs 1 and 5) and LiCl-KCl-$CaCl_2$ (runs 4 and 6) eutectics

Run	Eutectic Salt	$BiCl_3$ mol%	OCP/ (V vs. Ag/AgCl*)	$E^{o'}$/ (V vs. Ag/AgCl*)	$E^{o'}$/ (V vs. Cl^-/Cl_2)
1	LiCl-KCl	0.242 ± 0.0290	-0.0965 ± 0.0003	0.0214 ± 0.0025	-1.025 ± 0.0025
4	LiCl-KCl-$CaCl_2$	0.276 ± 0.0331	-0.0832 ± 0.002	0.0315 ± 0.0046	-1.015 ± 0.0046
5	LiCl-KCl	0.352 ± 0.0640	0.0061 ± 0.00007	0.1174 ± 0.004	-0.9266 ± 0.004
6	LiCl-KCl-$CaCl_2$	0.354 ± 0.0644	0.0083 ± 0.0001	0.1183 ± 0.004	-0.9255 ± 0.004
*Runs 1 and 4 used a mullite tube and 4.5 mol% AgCl, runs 5 and 6 used a pyrex tube and 4.75 mol% AgCl					

The $E^{o'}$ values are converted to Cl^-/Cl_2 reference potentials using the data from Yoon et al. [44]. The $E^{o'}(Bi^{3+}/Bi)$ value for run 1 of -1.025 V vs. Cl^-/Cl_2 at 681 K differs from the $E^{o'}(Bi^{3+}/Bi)$ value of -0.886 V vs. Cl^-/Cl_2 at 723 K reported by Plambeck by 0.140 V [1]. The $E^{o'}(Bi^{3+}/Bi)$ value for run 5 of -0.9266 V vs. Cl^-/Cl_2 at 681 K differs by 0.041 V from the $E^{o'}(Bi^{3+}/Bi)$ by Plambeck. The difference between the OCP measured for runs 1 and 5 is most likely due to a larger junction potential being experienced by the RE with a mullite tube. Some of the difference between the $E^{o'}$ values of run 5 and reported by Plambeck is due to the difference in temperatures ($\Delta T = 42$ K). In a data review, Zhang reported temperature dependencies of $E^{o'}$ ranging from 5.5 to 7.5 × 10^{-4} V K^{-1} for electrodeposition of lanthanides and actinides [45]. This correlates to potential differences of 0.023 to 0.032 V. The remaining 9-18 mV difference is reasonable and could be due to some minor differences in experimental procedures and equipment.

3.5 Cyclic Voltammetry

To determine how to minimize interference from peak C/C' in runs 2 and 3, CV measurements were conducted using different lower limits, as shown in Figure 8. When the lower limit was greater than -0.1 V, the W/$CaWO_4$ redox peaks (C/C') were not visible. At a lower limit of -0.2 V, the C_1/C' redox peak appears. At a lower limit of < -0.3 V, there are two visible oxidation peaks which could indicate two separate steps occurring for the W/$CaWO_4$ reaction. This second peak (C_2) is not discernable in Figure 4. However, both peaks C in Figure 4 and C_2 in Figure 8 start at -0.2 V. Hence, it is likely that C is C_1 and C_2 merged due to their larger size in Figure 4 where more reduced product was formed during the longer scan. The reduction behavior in the region of peaks B' and C' were also compared between runs 2 and 4, as shown in Figure 9. It can be seen in run 4 that no C' signal is evident. Semi-differential analysis can increase signal resolution, reduce background, and better distinguish overlapping signals [46–48]. Hence, the current density (i) in the top plot of Figure 9 was semi-differentiated (SD) resulting in taller and more narrow peaks, which decay to near zero current. Yet, there was still no evidence of peak C' in run 4 CV data, which typifies a single electrodeposition reaction on a foreign substrate (i.e., sharp rise with exponential decay following), as detailed elsewhere [48]. This confirms that the change in drying procedure (see Table 1) effectively removes the C' signal. The SD data also reveals that run 2 begins to depart from the typical SD response at about -0.1 V due to commencement of C' peak. Hence, CV measurements used to determine the diffusivity of Bi^{3+} used a lower limit ≥ -0.1 V. For each run, a set of CV measurements were conducted at varying scan rates. Some representative CV measurements are shown in Figure 10.

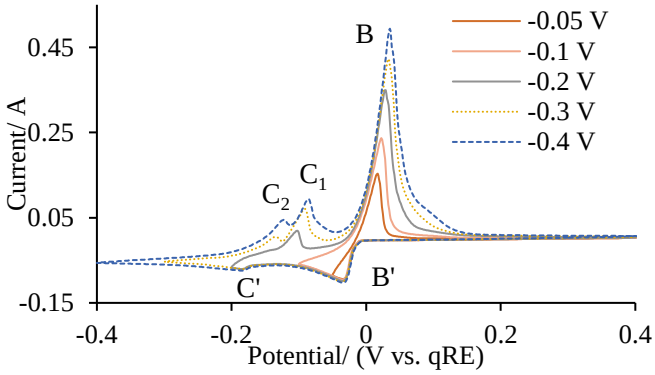

Fig. 8 CV curves for $BiCl_3$ at 4.24×10^{-5} mol cm^{-3} in molten LiCl-KCl-$CaCl_2$ eutectic at various lower potential limits. WE: 1.5 mm W rod, qRE: 1.5 mm W rod, CE: 3.175 mm W rod, WE Area: 1.374 cm^2, scan rate: 0.3 V s^{-1}, IR compensation: 0.18 Ω/78%

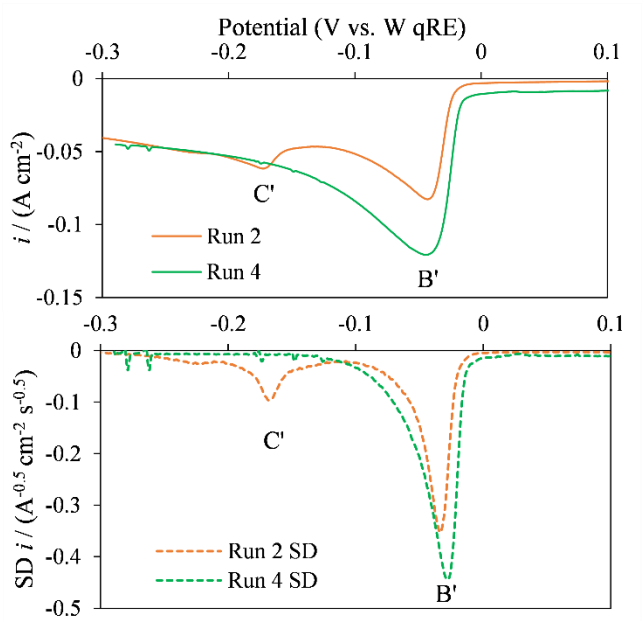

Fig. 9 Comparison of CV curves from run 2 (4.24×10^{-5} mol cm^{-3} $BiCl_3$) and run 4 (7.75×10^{-5} mol cm^{-3} $BiCl_3$) in molten LiCl-KCl-$CaCl_2$ eutectic. WE: 1.5 mm W rod; qRE: 1.5 mm W rod; CE: 3.175 mm W rod; WE Area: 1.374 cm^2 (run 2), 0.748 cm^2 (run 4); scan rate: 0.3 V s^{-1}; IR compensation: 0.18 Ω/78% (run 2), 0.4 Ω/77% (run 4)

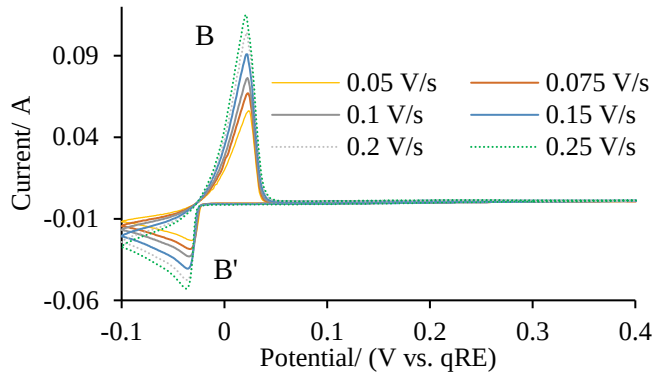

Fig. 10 CV curves of $BiCl_3$ at 4.24×10^{-5} mol cm^{-3} in molten LiCl-KCl-$CaCl_2$ eutectic at varying scan rates from run 3. WE: 1.5 mm W rod, qRE: 1.5 mm W rod, CE: 3.175 mm W rod, WE Area: 0.766 cm^2, IR compensation: 0.29 Ω/85%

The B/B' redox peaks in Figures 4, 8 and 10 exhibit the sharp peak shapes characteristic of insoluble metal deposition and stripping. Peak B rises exponentially when the reverse sweep crosses above the equilibrium potential due to preconcentration of deposited metal on the electrode surface, and then drops suddenly when the metal on electrode potential is oxidized off. Peak B grows in Figure 8 as the lower limit is extended more negatively due to the increased amount of metal deposited on the electrode during the prolonged duration at potentials more negative than the equilibrium potential.

Because the CV measurements are for the deposition of a metal (i.e., bismuth) onto a foreign substrate (i.e., tungsten), the expressions derived by Krulic et al. are used to calculate the diffusion coefficient [49]. An explanation for the need for the Krulic et al. expression as opposed to the Berzins-Delahay equation, previously shown in Eq. (1), as well as a detailed explanation of the equations used to calculate the diffusion coefficient from Krulic et al.'s expressions were recently detailed elsewhere [50]. Krulic et al.'s expressions are for reversible, soluble-insoluble reactions. Hence, the range of scan rates to use for the diffusivity calculation was determined by estimating the range of scan rates, over which the bismuth electrodeposition reaction exhibited reversible behavior in each run.

A soluble-insoluble reaction can be determined to be electrochemically reversible (hereafter referred to as reversible) if the peak position is independent of scan rate and the peak height is linear with the square root of scan rate [51]. The top plot in Figure 11 shows the peak position plotted against the natural log of scan rate along with the theoretical slope of peak position for electrochemically irreversible reactions. This slope is calculated from the relationship derived by Delahay between the peak position and scan rate for irreversible reactions [52], as shown in Eq. (4).

$$E_p = E^{0\prime} + \frac{1}{b}\left(0.780 + \ln\sqrt{\frac{D_o b \upsilon}{k^0}}\right) \tag{4}$$

E_p represents peak position, k^0 is the standard rate constant, and b is given by:

$$b = \frac{\alpha nF}{RT} \quad (5)$$

where α is the charge transfer coefficient, and all other variables are the same as defined previously. Eq. (4) can be simplified to isolate the relationship between the peak potential and the natural log of scan rate as shown in Eq. (6):

$$E_p = \frac{1}{2b}(\ln \upsilon) + P \quad (6)$$

where P is the contribution of all the other terms that can be separated from the scan rate term. This theoretical slope was used to estimate the extent of peak position shift expected for an irreversible reaction. The theoretical irreversible line in the top plot of Figure 10 was set to start at the same peak position as the lowest scan rate used to allow for easy comparison. The intercept is arbitrary and is not related to the P from Eq. (6).

It should be noted that values for α could range from near 0 to 1. Values for α from 0.015 to 0.67 have been estimated in molten salt electrodeposition studies [22, 53–55]. However, Laitinen et al. estimated α to be 0.5 for Bi^{3+}/Bi at a tungsten electrode [22]. Hence, an α of 0.5 was assumed in calculating the theoretical slope. As seen in Figure 11, the position shift for peak B' with increasing scan rate is minimal in comparison to the theoretical irreversible slope, which precludes the possibility of irreversibility.

To determine whether the reaction was reversible or quasi-reversible at this range of scan rates, the relationship between the peak height and square root of scan rate is examined. Quasi-reversible reaction peak heights are not linear with the square root of scan rate. Linearity is only maintained for reversible and irreversible reactions. The bottom plot of Figure 11 shows the peak height trend with square root of scan rate for runs 1-4. The theoretical reversible slope was determined using the slope regressed for the scan rate range of 0.05 – 0.15 V s^{-1} as this included the slowest scan rates that are most likely to be reversible. Runs 1-3 appear to be reversible over a large portion of the applied scan rates. Run 4 deviates from the theoretical reversible slope at scan rates greater than 0.15 V s^{-1}. This deviation could be due to the larger IR resistance measured for run 4. Though run 4 is compensated at a similar percentage as the other runs, the magnitude of the uncompensated resistance is higher due to the larger IR resistance value. To minimize the impact of uncompensated resistance and to be consistent, a scan rate range of 0.05 – 0.3 V s^{-1} was used to determine the diffusivity from each run.

Figure 12 plots the peak height against the square root of scan rate linear relationships obtained along with the raw data for the CV experiments conducted at 0.05 – 0.3 V s^{-1}. Table 5 shows the slopes obtained along with the calculated diffusivities. The diffusivity is calculated using an open-source, online tool, which uses relations from Krulic et al. to account for deposition onto a foreign substrate and a digital staircase approximation of an analog scan [49, 56]. The difference in the calculated diffusivity values could be due to several factors. The calcium tungstate reaction could be affecting the diffusivity values calculated for runs 2-3 even though precautions were taken to avoid the calcium tungstate peak. Alternatively, the difference in measured IR resistance, levels of compensation, and WE surface areas could have different effects on the reported values. However, the significance of the differences is uncertain as the 95% CIs overlap for the D_o values calculated in each run.

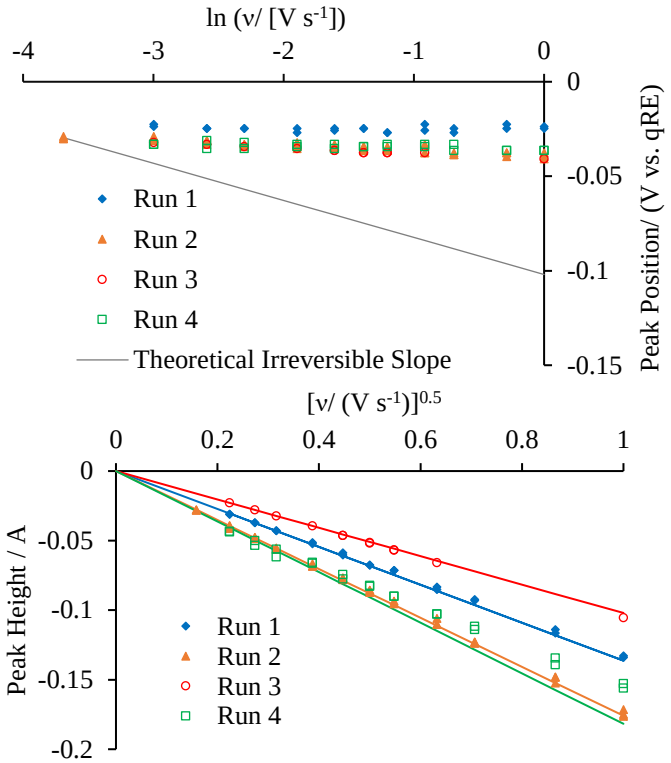

Fig. 11 Top: Peak position (markers) trend with scan rate for runs 1-4 with theoretical irreversible slope (line) plotted for comparison. Bottom: Peak heights (markers) plotted against the square root of scan rate for runs 1-4 with theoretical reversible lines included for comparison. WE: 1.5 mm W rod; qRE: 1.5 mm W rod; CE: 3.175 mm W rod; WE Area: 0.670 cm^2 (run 1), 1.374 cm^2 (run 2), 0.766 cm^2 (run 3), 0.748 cm^2 (run 4); IR compensation: 0.25 Ω/ 75% (run 1), 0.18 Ω/78% (run 2), 0.25 Ω/85% (run 3), 0.4 Ω/77% (run 4)

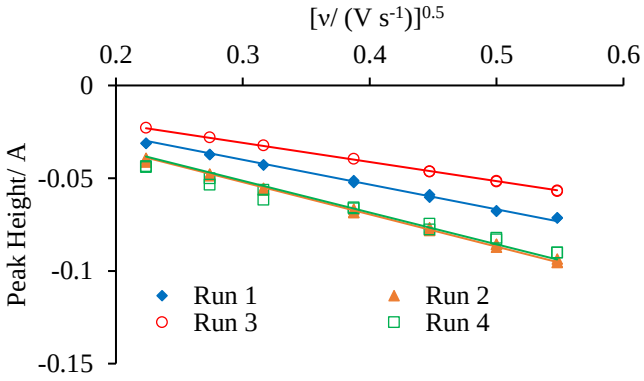

Fig. 12 Selected CV data (markers) with linear fits (lines) for calculating the diffusivity from runs 1-4. WE: 1.5 mm W rod; qRE: 1.5 mm W rod; CE: 3.175 mm W rod; WE Area: 0.670 cm^2 (run 1), 1.374 cm^2 (run 2), 0.766 cm^2 (run 3), 0.748 cm^2 (run 4); IR compensation: 0.25 Ω/ 75% (run 1), 0.18 Ω/78% (run 2), 0.25 Ω/85% (run 3), 0.4 Ω/77% (run 4)

Table 5 Slopes and calculated diffusivities from the CV measurements conducted for runs 1-4 for $BiCl_3$ in the LiCl-KCl and LiCl-KCl-$CaCl_2$ molten salt eutectics

Run	Eutectic Salt	Slope /(A $V^{-0.5}$ $s^{0.5}$)	D_o /(10^{-6} cm^2 s^{-1})
1	LiCl-KCl	-0.134 ± 0.001	6.56 ± 2.09
2	LiCl-KCl-$CaCl_2$	-0.174 ± 0.001	7.51 ± 1.94
3	LiCl-KCl-$CaCl_2$	-0.103 ± 0.0005	8.11 ± 2.15
4	LiCl-KCl-$CaCl_2$	-0.171 ± 0.006	8.91 ± 2.96

3.6.Chronoamperometry

CA experiments were also conducted to determine the diffusion coefficient of $BiCl_3$ in the LiCl-KCl and LiCl-KCl-$CaCl_2$ eutectics. A potential is applied that is far enough below the equilibrium potential to quickly reach the mass transfer limiting current before significant WE area growth occurs and/or natural convection influences the response. Once the mass transfer current limit is reached, the Cottrell equation, shown in Eq. (7), can be used to calculate the diffusion coefficient.

$$I = \frac{nFAC_o^*\sqrt{D_o}}{\sqrt{\pi t}} \tag{7}$$

Where I represents the current, t represents time, and all other variables were previously defined. The region of applied voltages that lead to mass transfer limiting currents was determined by graphing the CA data between -0.05 and -0.25 V to see at what applied voltages the current response remains the same with increasing applied voltage. Figure 13 shows CA measurements taken from -0.05 to -0.25 V for runs 1 and 2. In the top graph (run 1) in Figure 13 the data starts to overlap after 0.6 s for applied voltages <-0.1 V. In the bottom graph (run 2), the data has three intervals of applied voltages, one from -0.11 to -0.13 V, another from -0.19 to -0.21 V, and the last one from -0.23 to -0.25 V where it overlaps. From the CV results shown in Figures 8 and 9, it is possible that any potential <-0.1 V could be influenced by the calcium tungstate reduction. It is proposed for run 2 that the applied voltages greater than -0.11 V were not high enough to reach the mass transfer limiting current while the applied voltages less than -0.13 V were affected by the calcium tungstate reduction. With a stark jump in current being seen at an applied voltage of -0.15 V. The measured CA data for run 4 had similar behavior to that of run 1 while the measured CA data for run 3 had similar behavior to that of run 2. Further confirming that the calcium tungstate reduction was not noticeably affecting the measurements for run 4.

Based on the data from Figure 13 for run 1, a range of 0.6 to 1 s was used as the mass transfer limiting region as the data overlaps at applied voltages < -0.1 V over that time range. The CA data from 0.6 to 1 s was graphed against the inverse square root of time for each experiment. A linear fit for each data set was then determined using Microsoft© Excel. The slope from the linear fit was then used to calculate the diffusion coefficient for $BiCl_3$ for each CA measurement. The obtained diffusivities are plotted against the applied voltages in Figure 14.

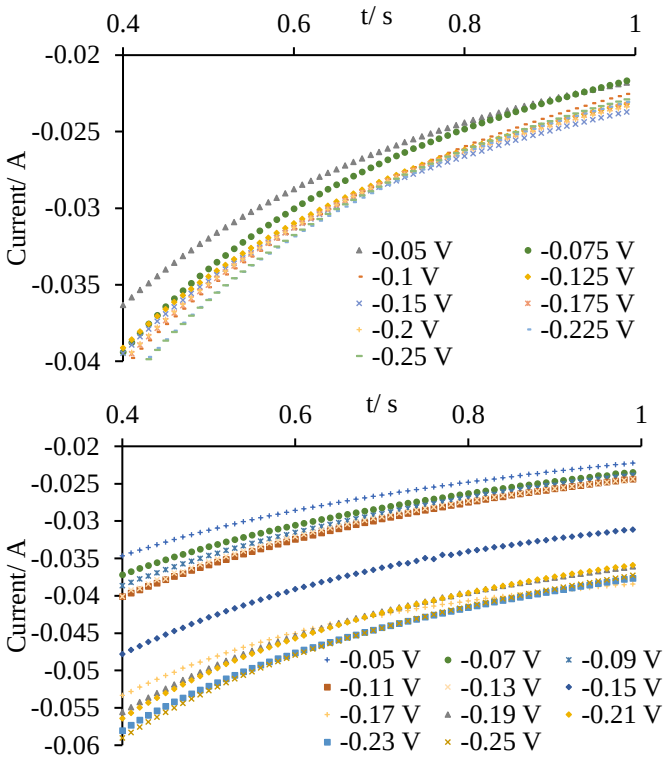

Fig. 13 Top: CA data from run 1 in the LiCl-KCl eutectic; Bottom: CA data from run 2 in the LiCl-KCl-$CaCl_2$ eutectic. WE: 1.5 mm W rod; qRE: 1.5 mm W rod; CE: 3.175 mm W rod; WE Area: 0.670 cm^2 (run 1), 1.374 cm^2 (run 2); IR compensation: 0.25 Ω/ 75% (run 1), 0.18 Ω/78% (run 2)

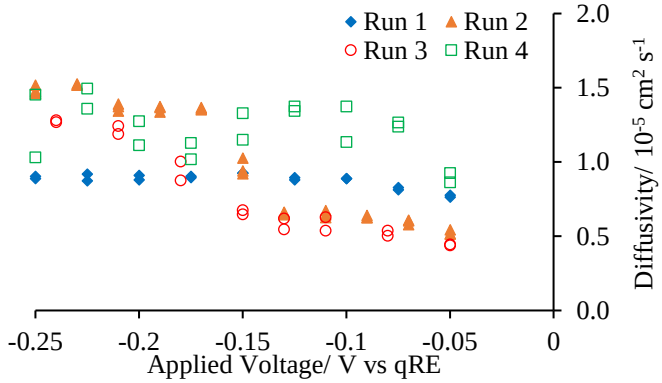

Fig. 14 Calculated diffusivities from the CA experiments from runs 1-4. WE: 1.5 mm W rod; qRE: 1.5 mm W rod; CE: 3.175 mm W rod; WE Area: 0.670 cm^2 (run 1), 1.374 cm^2 (run 2), 0.766 cm^2 (run 3), 0.748 cm^2 (run 4); IR compensation: 0.25 Ω/ 75% (run 1), 0.18 Ω/76% (run 2), 0.25 Ω/85% (run 3), 0.4 Ω/77% (run 4)

The applied voltage range used for calculating the average diffusivity value in each run was determined by selecting the flattest region of the curves shown in Figure 14. The applied voltage ranges, average slopes, and calculated diffusivities are shown in Table 6. These values from each run differ from one another. However, the significance of the difference is uncertain since the 95%

CIs overlap again and are larger than those calculated in CV measurements. The values from runs 2 and 3 are suspect due to potential interference from the C/C' signal. A truly diffusion limited current may not have been achieved in the -0.11 to -0.13 V range before it started to rise again in the -0.13 to -0.19 V range for runs 2-3. Alternatively, runs 1 and 4 had higher concentrations resulting in a higher diffusion limited current density, which increases the likelihood of surface area growth during CA. However, as seen in Fig. 13 (top), there is no discernable evidence for surface area growth (e.g., increasing current magnitude, jagged signal). Another possible reason for the inflated diffusivities is nucleation effects causing the experimental data to deviate from Cottrellian behavior [57, 58].

Table 6 Voltage ranges, average slopes, and diffusivities from the CA experiments from runs 1-4 for $BiCl_3$ in the LiCl-KCl and LiCl-KCl-$CaCl_2$ molten salt eutectics

Run	Eutectic Salt	Applied Voltages /V	Slope /(A $s^{0.5}$)	D_o /(10^{-6} cm^2 s^{-1})
1	LiCl-KCl	-0.175 to -0.25	-0.0235 ± 0.0004	8.96 ± 3.19
2	LiCl-KCl-$CaCl_2$	-0.09 to -0.13	-0.0242 ± 0.0007	6.44 ± 2.07
3	LiCl-KCl-$CaCl_2$	-0.11 to -0.13	-0.0128 ± 0.0010	5.82 ± 2.71
4	LiCl-KCl-$CaCl_2$	-0.15 to -0.25	-0.0332 ± 0.0046	12.3 ± 8.91

3.7. Chronopotentiometry

The last method used to determine the diffusivity of $BiCl_3$ in the LiCl-KCl and LiCl-KCl-$CaCl_2$ eutectics was CP. A current is applied and the potential changes with time. The potential drops precipitously when the mass transfer limiting current of the initial reaction is exceeded. An additional reaction is needed to be able to supply the demanded current and the voltage changes to reflect that. Because of this, the current applied must be high enough that the mass transfer limit of the initial reaction is reached and surpassed. The time at which the mass transfer limit is reached, referred to as the transition time (τ), can be related to the diffusivity using the Sand equation shown in Eq. (8):

$$\frac{i\tau^{0.5}}{C_O^*} = \frac{nFA\sqrt{D_O\pi}}{2} \tag{8}$$

where all the variables are defined previously. The derivation of this relationship is covered in a review on different methods for determining electrolyte concentration [59]. Fig. 13 shows example CP measurements from runs 1 and 3. The CP measurements from run 1 and 4 all looked similar to the top plot in Figure 15 (i.e., typical CP response) and a τ could be determined. The CP measurements from runs 2 and 3 all looked similar to the bottom plot in Figure 15, in which an initial voltage drop occurs just after 2 seconds. This voltage drop is associated with the first reaction (Bi^{3+}/Bi) beginning to approach mass transfer limitation. However, the voltage begins to level out before the voltage drop is completed. This is due to the commencement of calcium tungstate reduction. The voltage drop not being completed shows that there is not enough separation in the potentials of the bismuth electrodeposition and calcium tungstate reduction reactions to distinguish separate τ values. Due to the inability to determine τ from the obtained data, no diffusivity is reported from the CP experiments for runs 2 and 3. The top plot in Figure 15 demonstrates how τ was determined graphically. The two linear portions were fit using Microsoft© Excel and the intercept of the two lines was then used as τ. When using this methodology, the error in determining τ was estimated to be less than 10%.

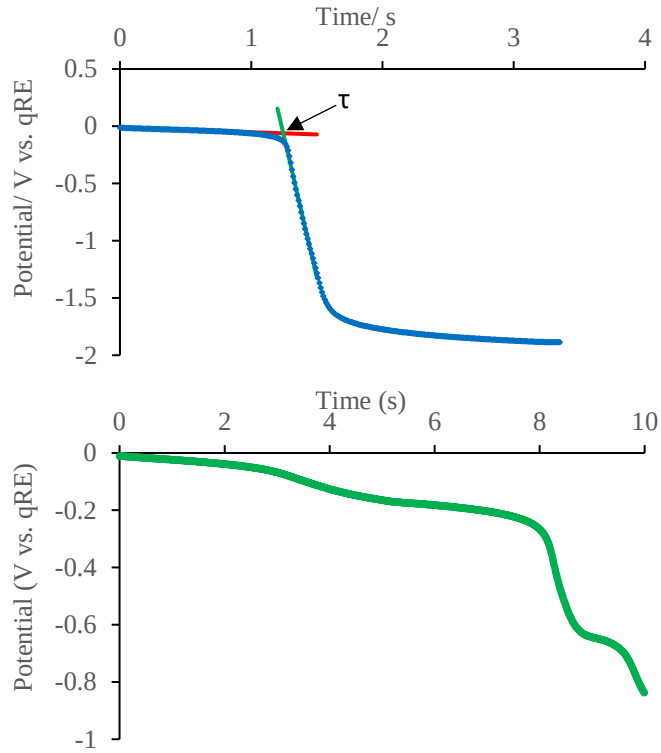

Fig. 15 Example CP experiments of $BiCl_3$ in Top: the LiCl-KCl eutectic at an applied current of -0.03 A from run 1 and Bottom: the LiCl-KCl-$CaCl_2$ eutectic at an applied current of -0.01 A from run 3. WE: 1.5 mm W rod; qRE: 1.5 mm W rod; CE: 3.175 mm W rod; WE Area: 0.670 cm^2 (run 1), 0.766 cm^2 (run 3); IR Comp: N/A

Figure 16 shows the calculated diffusivities from the CP measurements for each of the applied currents from runs 1 and 4. The calculated diffusivities at the lowest applied currents were greater than those from the other experiments. This could be due to surface area growth and/or natural convection starting to affect the measurement due to the longer τ values (3-3.8 s) associated with the lower applied currents. The variance between the two measurements at an applied current of -0.06 A in both runs 1 and 4 was greater than the measurements at the other applied currents. The first CP measurement conducted for both runs 1 and 4 was at -0.06 A and was the one that differed from the other measurements. Due to this, the first CP measurement at -0.06 A was not used to calculate the diffusivity from the CP measurements. The current ranges used to calculate the diffusivity were based on the linearity of the current against the inverse square root of τ. The graphs of this relationship for the applied current ranges selected are shown in Figure 16. The slopes from these graphs were used to calculate the diffusivity based on the Sand equation shown in Eq. (8). The selected applied current ranges, and calculated diffusivities are shown in Table 7. As was the case for CV, the diffusivity calculated for run 4 is greater than run 1 by a similar amount.

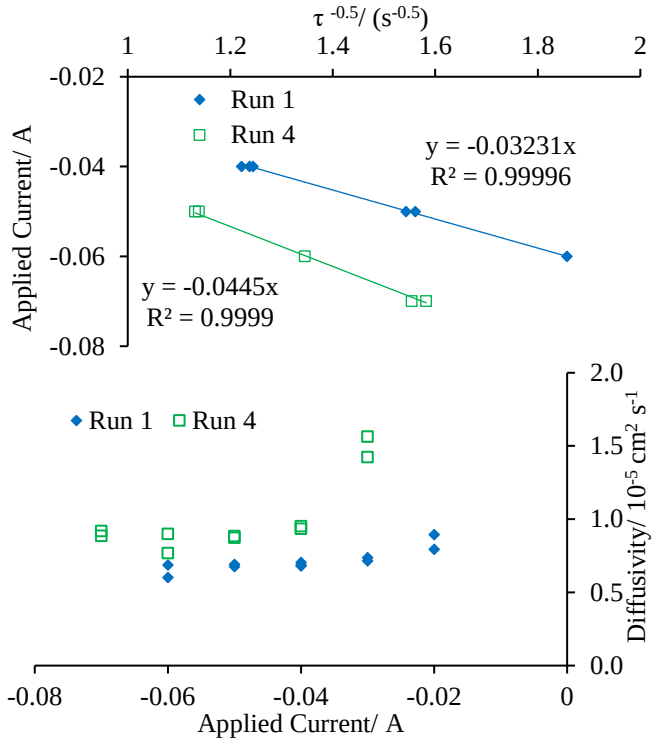

Fig. 16 Top: The applied currents plotted against the inverse square root of τ for runs 1 and 4. Bottom: Diffusion coefficients of $BiCl_3$ determined from the CP experiments in the LiCl-KCl eutectic (run 1) and the LiCl-KCl-$CaCl_2$ eutectic (run 4). WE: 1.5 mm W rod; qRE: 1.5 mm W rod; CE: 3.175 mm W rod; WE Area: 0.670 cm^2 (run 1), 0.748 cm^2 (run 4); IR Comp: N/A

Table 7 Applied current ranges and calculated diffusivities from the CA experiments from runs 1 and 4 for $BiCl_3$ in the LiCl-KCl and LiCl-KCl-$CaCl_2$ molten salt eutectics

Run	Eutectic Salt	Applied Currents /A	Diffusivity /(10^{-6} cm^2 s^{-1})
1	LiCl-KCl	-0.04 to -0.06	6.85 ± 2.25
4	LiCl-KCl-$CaCl_2$	-0.05 to -0.07	8.95 ± 3.26

3.8.Compiled Diffusivity Values

The diffusivity values calculated for each run and method are compiled in the bar chart in Figure 17. As discussed in previous sections, the diffusivity values for runs 2 and 3 are suspect due to the inability to confidently rule out potential interference from peak C'. Diffusivity values from run 4 are deemed more reliable for the LiCl-KCl-$CaCl_2$ system due to a lack of evidence for peak C' in any of the methods. The diffusivity values calculated using CA data differed considerably, but still within error, from the values from other methods across all the runs. CA measurements can be affected by IR drop, WE surface area growth, nucleation, and/or natural convection. The Cottrell equation, Eq. (7), does not account for any of these effects. Optimizing the time range used for analysis could minimize these effects. However, these effects are in competition with each other. WE surface area growth and natural convection are minimized at shorter times. While IR drop and nucleation have less of an impact at longer times [59]. Indeed, "the current… is not well described by the simple Cottrell equation in the case of slow nucleation, except at sufficiently long times"

[57]. Further refinement of CA measurements and analysis is suggested to minimize and/or account for non-diffusional effects when determining the diffusivity in molten salts.

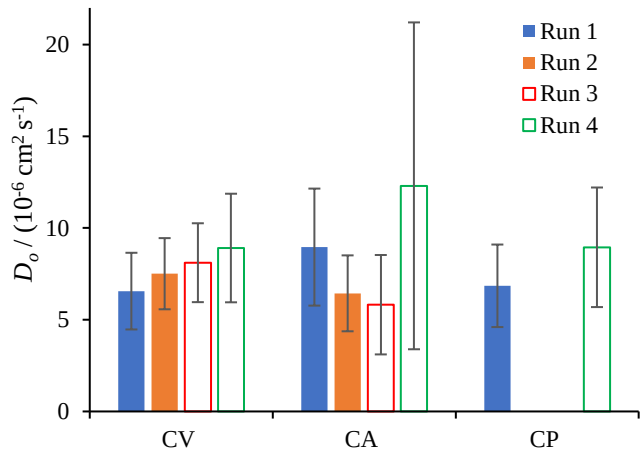

Fig. 17 Experimentally determined diffusivities and their associated 95% confidence intervals (error bars) from the CV, CA, and CP experiments for run 1 (LiCl-KCl) and runs 2-4 (LiCl-KCl-$CaCl_2$) for $BiCl_3$ in molten salt eutectics

The diffusivities for runs 1 and 4 determined from the CV and CP measurements are the most trusted values and recommended by the authors for the diffusivity of bismuth ions in the bismuth electrodeposition reaction in LiCl-KCl and LiCl-KCl-$CaCl_2$ eutectics, respectively. The authors acknowledge that there is a high level of uncertainty but are encouraged by the consistency in the data between two different methods (i.e., CV, CP). The recommended diffusivity values for the LiCl-KCl eutectic is approximately one third of the diffusivity reported by Carlin et. al. [2] of 2.2 x 10^{-5} cm^2/s at 673 K for Bi^{3+}. Carlin et al. calculated the diffusivity using the relationship between the limiting current (I_{lim}) from normal pulse voltammetry (essentially a series of CA measurements) and pulse time (t_p). Since a micro disk WE was used, the plot of the I_{lim} with $t_p^{-1/2}$ should be linear with a positive y-intercept. However, Carlin et al. noted that the intercept of I_{lim} vs. $t_p^{-1/2}$ plot was negative introducing some error to their calculation. The CA data in this work also had non-zero intercepts indicating that Cottrellian behavior may not have been fully achieved, which may have led to higher calculated values for the diffusivity than the CV and CP method. Diffusivity decreases with decreasing temperature and it is not uncommon to determine diffusivities on the order of 10^{-6} cm^2 s^{-1} at 723 K and below in molten LiCl-KCl eutectic [45, 60–63]. For example, Gd^{3+} has diffusivities ranging from 5.2 to 6.5 × 10^{-6} cm^2 s^{-1} at 681 K in molten LiCl-KCl eutectic [45, 60, 61]. This is encouraging considering that the ionic radii of Gd^{3+} (97 pm) and Bi^{3+} (96 pm) are similar.

The ionic radius (or particle size) is a key property influencing diffusivity of an ion according to the Stokes-Einstein model. In a dilute solution of species '*o*', the Stokes-Einstein equation predicts the diffusivity as follows:

$$D_o = \frac{k_B T}{6\pi\mu a} \tag{9}$$

where k_B is the Boltzman's constant, μ is the dynamic viscosity, and a is the atomic or particle radius. The Stokes-Einstein equation "has been shown to be exact for large, spherical particles…

and is surprising accurate for solute radii as small as two to three times that of the solvent" [64]. Hence, the radius of the diffusing solute will impact the diffusivity according to the Stokes-Einstein equation.

Notwithstanding the significant uncertainty to the calculated values in Figure 17, there is a consistent trend of the diffusivity value from run 4 being larger than the value from run 1 in Figure 17 across the methods. This trend could be due to the LiCl-KCl-$CaCl_2$ eutectic having a lower melting point than LiCl-KCl eutectic (See Figure 1). The lower melting point of LiCl-KCl-$CaCl_2$ eutectic could result in it having a lower viscosity than LiCl-KCl eutectic at the same temperature. Unfortunately, the authors were unable to find viscosity data to support this hypothesis. However, the hypothesis is supported by the Stokes-Einstein model and the principles of corresponding states.

The Stokes-Einstein equation, Eq. (9), illustrates that diffusivity will increase with temperature. However, often, the decrease in viscosity with increasing temperature has a greater effect on increasing D_o [64]. The properties of fluids, including viscosity, can be estimated and general trends explored by employing principles of corresponding state, where properties are compared to the same reduced state [65]. The critical point is often used to obtain the reduced state. However, data is lacking for the critical point of eutectic salts. Hence, the melting point of molten salts will be used instead as the reduced state (i.e., reduced temperature) to illustrate corresponding-states correlations.

The viscosity of a liquid (including ionic liquids [66] and molten salts [67]) decreases with increasing temperature, generally following an Arrhenius relationship:

$$\mu = \beta e^{\gamma/T} \tag{10}$$

where β and γ are adjustable parameters. If the reduced state is taken as the melting point of the molten salt, then the extrapolated reduced state viscosity (μ_m) can be calculated as follows:

$$\mu_m = \beta e^{\gamma/T_m} \tag{11}$$

where T_m is the melting (or liquidus) temperature of the molten salt. Normalizing viscosity and temperature by their respective reduced state values should result in viscosity values from a variety of molten salts to collapse to a single dependency.

To demonstrate the validity and estimating ability of corresponding states for the viscosity of molten salts, the natural log of μ normalized by μ_m is plotted against the inverse of the reduced state temperature (T_m/T) for a few salt systems [35] in Figure 18. For the LiCl-KCl (60:40 mol%) and equimolar $CaCl_2$-NaCl salts, T_m was determined from the liquidus line at the appropriate composition in the respective phase diagrams [68]. Each system has a trend of decreasing μ as T increases (i.e., T_m/T decreases). Furthermore, the normalized viscosities of each system lie close to the overall trend (black dotted line in Figure 18) of the data from all salt systems. Hence, the general trend for the viscosity of molten salts is decreasing as the temperature difference between T and T_m increases (i.e., T_m/T decreases). If the LiCl-KCl and LiCl-KCl-$CaCl_2$ eutectics have a similar μ_m, then moving from the LiCl-KCl eutectic (T_m = 628 K) to the LiCl-KCl-$CaCl_2$ eutectic

(T_m = 612 K) would decrease T_m/T from 0.92 to 0.90, which would result in a 5% decrease in μ and an inversely proportional increase in D_o according to Eq. (9).

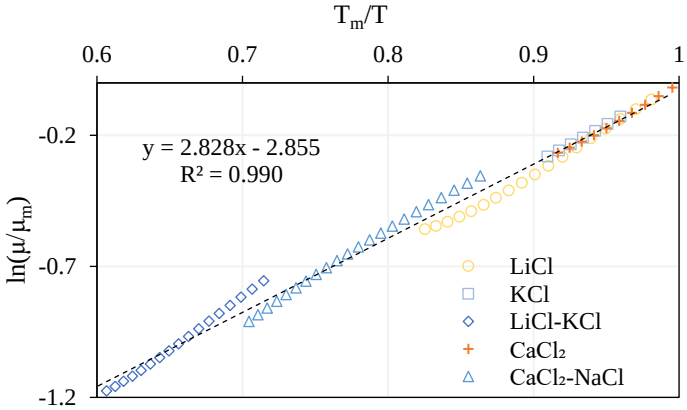

Fig. 18 Plot of reduced viscosity data from Ref. [35] for LiCl, KCl, $CaCl_2$, LiCl-KCl (60:40 mol%), equimolar $CaCl_2$-NaCl after being normalized by reduced state values. The dotted black line is the overall trend across datasets.

There is significant uncertainty in regard to the trends and values of D_o. The most significant contributor to the uncertainty is the ICP-MS measured concentration of Bi, which varied considerably across samples. The source of this uncertainty is undetermined. Several sources could be explored to further improve the accuracy of ICP-MS analysis of samples taken from molten salts including, but not limited to, sampling methods (e.g., number and size of samples, techniques), digestion chemistry, and sample preparation methods (e.g., internal standards, standard addition, bracketing). For example, $BiCl_3$ has complex dissolution behavior and requires the presence of HCl to avoid precipitating some hydrolyzed $BiCl_3$ as BiOCl [69, 70]. Initially, salt samples were dissolved solely in nitric acid. However, upon the addition of HCl, more consistent ICP-MS measurements of Bi concentrations were obtained, but significant variation persisted as illustrated by the error reported herein. Based on the last author's experience in conducting a review of the literature [59], the uncertainty introduced from sampling, digesting, diluting, and other steps in performing ICP-MS analysis are often not addressed in molten salt electrochemical studies. Our study highlights the need to devote greater attention towards minimizing and verifying ICP-MS measurement errors to improve the accuracy of determined properties, especially diffusivities.

4. Conclusions

The electrochemical parameters for $BiCl_3$ in the LiCl-KCl and LiCl-KCl-$CaCl_2$ eutectics have been determined using CV, SWV, CA, CP, and OCP measurements. The bismuth electrodeposition reaction was confirmed to be a three-electron exchange process using SWV. The standard redox potential for the Bi^{3+}/Bi couple was measured to be 0.1166 V vs. Ag/AgCl (4.75 mol%) and 0.1187 V vs. Ag/AgCl (4.75 mol%) in the molten LiCl-KCl and LiCl-KCl-$CaCl_2$ eutectics, respectively, at 680 ± 2.1 K using REs with a pyrex membrane. The RE membrane had a significant influence on the OCP observed at the temperatures (678-681K) of this study in both eutectic melts. Diffusivity values of 6.71 x 10^{-6} cm^2 s^{-1} and 8.93 x 10^{-6} cm^2 s^{-1} were recommended for $BiCl_3$ in the LiCl-KCl and LiCl-KCl-$CaCl_2$ eutectics. These values were determined by averaging the CV and CP results for runs 1 and 4, respectively. A significant amount of uncertainty (± ~30%) was introduced to the calculated diffusivities, primarily from errors associated with the

ICP-MS analysis of Bi content. Nonetheless, the estimated diffusivities for bismuth in LiCl-KCl and LiCl-KCl-$CaCl_2$ eutectics improve upon the previous lack of values and associated error estimates at the conditions of this study (678-686 K). Diffusivities were calculated for runs 2 and 3, but interference from $CaWO_4$ signal could not be ruled out, which introduced an unknown amount of uncertainty. The drying method for $CaCl_2$ was improved for runs 4-6 and no evidence of the $CaWO_4$ signal was observed. D_o values calculated from CA data were found to be inconsistent with CV and CP in estimating diffusivity. For future work, it is recommended to further refine the CA method and analysis so that diffusivity values in molten salts can be further validated. This may involve analyzing the effects of non-faradaic currents, WE area growth, natural convection, nucleation, and different amounts of IR compensation. Furthermore, uncertainties associated with ICP-MS analysis need to be explored to identify and minimize sources of error.

Acknowledgments

This work was performed under the auspices of the U.S. Department of Energy by Lawrence Livermore National Laboratory under Contract DE-AC52-07NA27344.

References

1. Plambeck JA (1967) Electromotive force series in molten salts. J Chem Eng Data 12:77–82. https://doi.org/10.1021/je60032a023

2. Carlin RT, Osteryoung RA (1989) Deposition Studies of Lithium and Bismuth at Tungsten Microelectrodes in LiCl : KCl Eutectic. J Electrochem Soc 136:1249–1255. https://doi.org/10.1149/1.2096900

3. Chipman G, Johnson B, Choi S, et al (2023) Determination of a surrogate for plutonium electrorefining. Journal of Nuclear Materials 586:154680. https://doi.org/10.1016/j.jnucmat.2023.154680

4. Fredrickson GL, Yoo T-S (2020) Liquid cadmium cathode performance model based on the equilibrium behaviors of U and Pu in molten LiCl–KCl/Cd system at 500°C. Journal of Nuclear Materials 528:151883. https://doi.org/10.1016/j.jnucmat.2019.151883

5. Yin T, Liu Y, Yang D, et al (2020) Thermodynamics and Kinetics Properties of Lanthanides (La, Ce, Pr, Nd) on Liquid Bismuth Electrode in LiCl-KCl Molten Salt. J Electrochem Soc 167:122507. https://doi.org/10.1149/1945-7111/abb0f4

6. Yang D-W, Liu Y-L, Yin T-Q, et al (2020) Application of Binary Ga–Al Alloy Cathode in U Separation from Ce: The Possibility in Pyroprocessing of Spent Nuclear Fuel. Electrochimica Acta 353:136449. https://doi.org/10.1016/j.electacta.2020.136449

7. Koyama T, Iizuka M (2015) 18 - Pyrochemical fuel cycle technologies for processing of spent nuclear fuels: Developments in Japan. In: Taylor R (ed) Reprocessing and Recycling of Spent Nuclear Fuel. Woodhead Publishing, Oxford, pp 457–519

8. Lewin RG, Harrison MT (2015) 15 - International developments in electrorefining technologies for pyrochemical processing of spent nuclear fuels. In: Taylor R (ed) Reprocessing and Recycling of Spent Nuclear Fuel. Woodhead Publishing, Oxford, pp 373–413

9. Zhang H, Du Q, Du X, et al (2023) Selective extraction of Sm from LiCl-KCl molten salt into wasteforms via liquid bismuth. Separation and Purification Technology 313:123441. https://doi.org/10.1016/j.seppur.2023.123441

10. Yoon J-H, Kim S-H, Kim G-Y, et al (2013) A study on the electrodeposition of uranium using a liquid cadmium cathode at 440℃ and 500℃. Journal of Nuclear Fuel Cycle and Waste Technology(JNFCWT) 11:199–206. https://doi.org/10.7733/jnfcwt-k.2013.11.3.199

11. Kim S-H, Yoon D-S, You Y-J, et al (2009) In-situ observation of a dendrite growth in an aqueous condition and a uranium deposition into a liquid cadmium cathode in an electrowinning system. Journal of Nuclear Materials 385:196–199. https://doi.org/10.1016/j.jnucmat.2008.10.019

12. Yasuda K, Nohira T, Ogata YH, Ito Y (2005) Electrochemical window of molten LiCl–KCl–CaCl2 and the Ag+/Ag reference electrode. Electrochimica Acta 51:561–565. https://doi.org/10.1016/j.electacta.2005.05.014

13. Sri Maha Vishnu D, Sanil N, Mohandas KS, Nagarajan K (2016) Electrochemical characterisation of CaCl2 deficient LiCl–KCl–CaCl2 eutectic melt and electro-deoxidation of solid UO2. J Nucl Mater 470:179–186. https://doi.org/10.1016/j.jnucmat.2015.12.003

14. The American Ceramic Society and the National Institute of Standards and Technology (2023) Phase Equilibria Diagrams Online Database (NIST Standard Reference Database 31). In: Figure Number 16819. https://www.nist.gov/srd/nist-standard-reference-database-31

15. Yin T, Liu K, Liu Y, et al (2018) Electrochemical and Thermodynamic Properties of Uranium on the Liquid Bismuth Electrode in LiCl-KCl Eutectic. J Electrochem Soc 165:D722. https://doi.org/10.1149/2.0571814jes

16. Arkhipov PA, Zaikov YP, Khalimullina YR, Arkhipov SP (2021) Electrochemical Production of Bismuth in the KCl–PbCl2 Melt. Materials 14:5653. https://doi.org/10.3390/ma14195653

17. Jiang S, Liu K, Liu Y, et al (2019) Electrochemical behavior of Th(IV) on the bismuth electrode in LiCl–KCl eutectic. Journal of Nuclear Materials 523:268–275. https://doi.org/10.1016/j.jnucmat.2019.06.008

18. Serp J, Lefebvre P, Malmbeck R, et al (2005) Separation of plutonium from lanthanum by electrolysis in LiCl–KCl onto molten bismuth electrode. J Nucl Mater 340:266–270. https://doi.org/10.1016/j.jnucmat.2004.12.004

19. FNC Technology Co., Ltd., 46, Tapsil-ro, Giheung-gu, Yongin-si, Gyeonggi-do 17084, Republic of Korea, Kim BK, Park BG (2022) Electrochemical Behaviors of Bi^{3+} Ions on Inert Tungsten or on Liquid Bi Pool in the Molten LiCl-KCl Eutectic. J of Nucl Fuel Cycle and waste Technol 20:33–41. https://doi.org/10.7733/jnfcwt.2022.004

20. Castrillejo Y, Haarberg GM, Palmero S, et al (1994) Chemical and electrochemical behaviour of BiCl3 in a PbCl2 + KCl equimolar mixture at 475°C. Journal of Electroanalytical Chemistry 373:149–155. https://doi.org/10.1016/0022-0728(94)03313-7

21. Laitinen HA, Liu CH, Ferguson WS (1958) Polarography of Metal Ions in Fused Lithium Chloride-Potassium Chloride Eutectic. Anal Chem 30:1266–1270. https://doi.org/10.1021/ac60139a023

22. Laitinen HA, Tischer RP, Roe DK (1960) Exchange Current Measurements in KCl-LiCl Eutectic Melt. Journal of The Electrochemical Society 107:546. https://doi.org/10.1149/1.2427740

23. Schvaneveldt M, Fuller R, Rappleye D (2022) Electroanalytical measurements of lanthanum (III) chloride in molten calcium chloride and molten calcium chloride and lithium chloride. J Electroanal Chem 918:116442. https://doi.org/10.1016/j.jelechem.2022.116442

24. Schvaneveldt M (2022) In-Situ Chlorine Gas Generation for Chlorination and Purification of Rare Earth and Actinide Metals. Theses and Dissertations

25. Masset PJ (2009) Thermogravimetric study of the dehydration reaction of LiCl·H2O. J Therm Anal Calorim 96:439–441. https://doi.org/10.1007/s10973-008-9399-y

26. Molenda M, Stengler J, Linder M, Wörner A (2013) Reversible hydration behavior of CaCl2 at high H2O partial pressures for thermochemical energy storage. Thermochimica Acta 560:76–81. https://doi.org/10.1016/j.tca.2013.03.020

27. Shum R, Fuller M, Williams T, Rappleye D (2023) Electrochemical Investigation of Moisture Byproducts in Molten Calcium Chloride

28. Yang L, Hudson RG (1959) Some Investigations of the Ag⁄AgCl in LiCl-KCl Eutectic Reference Electrode. J Electrochem Soc 106:986. https://doi.org/10.1149/1.2427195

29. Yoon S, Kang D, Sohn S, et al (2020) Reference electrode at molten salt: A comparative analysis of electroceramic membranes. J Nucl Fuel Cycle Waste Technol 18:143–155. https://doi.org/10.7733/jnfcwt.2020.18.2.143

30. Agatemor C, Beauchemin D (2011) Matrix effects in inductively coupled plasma mass spectrometry: A review. Analytica Chimica Acta 706:66–83. https://doi.org/10.1016/j.aca.2011.08.027

31. Medvedev NS, Shaverina AV, Tsygankova AR, Saprykin AI (2018) Comparison of analytical performances of inductively coupled plasma mass spectrometry and inductively coupled plasma atomic emission spectrometry for trace analysis of bismuth and bismuth oxide. Spectrochimica Acta Part B: Atomic Spectroscopy 142:23–28. https://doi.org/10.1016/j.sab.2018.01.017

32. Wilschefski SC, Baxter MR (2019) Inductively Coupled Plasma Mass Spectrometry: Introduction to Analytical Aspects. Clin Biochem Rev 40:115–133. https://doi.org/10.33176/AACB-19-00024

33. Van Artsdalen ER, Yaffe IS (1955) Electrical Conductance and Density of Molten Salt Systems: KCl–LiCl, KCl–NaCl and KCl–KI. J Phys Chem 59:118–127. https://doi.org/10.1021/j150524a007

34. Robelin C, Chartrand P, Eriksson G (2007) A Density Model for Multicomponent Liquids Based on the Modified Quasichemical Model: Application to the NaCl-KCl-MgCl2-CaCl2 System. Metall Mater Trans B 38:869–879. https://doi.org/10.1007/s11663-007-9090-x

35. Janz GJ, Tomkins RPT, Allen CB, et al (1975) Molten salts: Volume 4, part 2, chlorides and mixtures—electrical conductance, density, viscosity, and surface tension data. Journal of Physical and Chemical Reference Data 4:871–1178. https://doi.org/10.1063/1.555527

36. Rappleye D, Horvath D, Wang Z, et al (2016) Methods for Determining the Working Electrode Interfacial Area for Electroanalytical Measurements of Metal Ions in Molten LiCl-KCl. ECS Trans 75:79. https://doi.org/10.1149/07515.0079ecst

37. Shen M, Li B, Yu J (2012) Investigation on electrochemical removal of CaCl2 from LiCl–KCl melts. Electrochimica Acta 62:153–157. https://doi.org/10.1016/j.electacta.2011.12.007

38. Zhang C, Rappleye D, Nelson A, et al (2021) Electroanalytical Measurements of Oxide Ions in Molten CaCl2 on W electrode. J Electrochem Soc 168:097502. https://doi.org/10.1149/1945-7111/ac208e

39. Kondo H, Asaki Z, Kondo Y (1978) Hydrolysis of fused calcium chloride at high temperature. Metall Trans B 9:477–483. https://doi.org/10.1007/BF02654424

40. Kim H, Smith N, Kumar K, Lichtenstein T (2016) Electrochemical Separation of Barium into Liquid Bismuth by Controlling Deposition Potentials. Electrochimica Acta 220:237–244. https://doi.org/10.1016/j.electacta.2016.10.083

41. Gschneidner KA, Calderwood FW (2016) ASM Alloy Phase Diagram Database. https://www.asminternational.org/materials-resources/online-databases/-/journal_content/56/10192/15469013/DATABASE. Accessed 28 Jan 2023

42. Fatouros N, Krulic D (2013) Analysis of the square wave voltammetry for reversible metal deposition on a foreign substrate – Experimental study of silver deposition on gold. J Electroanal Chem 706:76–85. https://doi.org/10.1016/j.jelechem.2013.07.019

43. Fuller R, Williams T, Schvaneveldt M, Rappleye D (2022) A comparison of square-wave voltammetry models to determine the number of electrons exchanged in metal deposition. Electrochimica Acta 414:140220. https://doi.org/10.1016/j.electacta.2022.140220

44. Yoon D, Baggett A, Phongikaroon S, et al (2019) Fundamental Data Acquisition toward Silver-Silver Chloride Reference Electrode. J Electrochem Soc 166:E159. https://doi.org/10.1149/2.0721906jes

45. Zhang J (2014) Electrochemistry of actinides and fission products in molten salts—Data review. J Nucl Mater 447:271–284. https://doi.org/10.1016/j.jnucmat.2013.12.017

46. Tylka MM, Willit JL, Prakash J, Williamson MA (2015) Application of Voltammetry for Quantitative Analysis of Actinides in Molten Salts. J Electrochem Soc 162:H852–H859. https://doi.org/10.1149/2.0281512jes

47. Rappleye D, Jeong S-M, Simpson M (2016) Electroanalytical Measurements of Binary-Analyte Mixtures in Molten LiCl-KCl Eutectic: Gadolinium(III)- and Lanthanum(III)-Chloride. J Electrochem Soc 163:B507. https://doi.org/10.1149/2.1011609jes

48. Williams T, Fuller R, Vann C, Rappleye D (2023) Semi-Differentiation of Reversible, Soluble-Insoluble Potential Sweep Voltammograms. J Electrochem Soc 170:042502. https://doi.org/10.1149/1945-7111/accc59

49. Krulic D, Fatouros N, Liu D (2015) A complementary survey of staircase voltammetry with metal ion deposition on macroelectrodes. Journal of Electroanalytical Chemistry 754:30–39. https://doi.org/10.1016/j.jelechem.2015.06.012

50. Rappleye DS, Fuller RG (2023) Bringing the Analysis of Electrodeposition Signals in Voltammetry Out of the Shadows. J Electrochem Soc 170:063505. https://doi.org/10.1149/1945-7111/acd879

51. Berzins T, Delahay P (1953) Oscillographic Polarographic Waves for the Reversible Deposition of Metals on Solid Electrodes. J Am Chem Soc 75:555–559. https://doi.org/10.1021/ja01099a013

52. Delahay P (1953) Theory of Irreversible Waves in Oscillographic Polarography. J Am Chem Soc 75:1190–1196. https://doi.org/10.1021/ja01101a054

53. Lim KH, Park S, Yun J-I (2015) Study on Exchange Current Density and Transfer Coefficient of Uranium in LiCl-KCl Molten Salt. J Electrochem Soc 162:E334–E337. https://doi.org/10.1149/2.0571514jes

54. Yoon D, Phongikaroon S (2017) Measurement and Analysis of Exchange Current Density for U/U3+ Reaction in LiCl-KCl Eutectic Salt via Various Electrochemical Techniques. Electrochim Acta 227:170–179. https://doi.org/10.1016/j.electacta.2017.01.011

55. Rappleye D, Simpson MF (2017) Application of the rotating cylinder electrode in molten LiCl-KCl eutectic containing uranium(III)- and magnesium(II)-chloride. J Nucl Mater 487:362–372. https://doi.org/10.1016/j.jnucmat.2017.02.037

56. Rappleye D (2023) Voltammetry

57. Heerman L, Tarallo A (1999) Theory of the chronoamperometric transient for electrochemical nucleation with diffusion-controlled growth. J Electroanal Chem 470:70–76. https://doi.org/10.1016/S0022-0728(99)00221-1

58. Tylka MM, Willit JL, Williamson MA (2017) Electrochemical Nucleation and Growth of Uranium and Plutonium from Molten Salts. J Electrochem Soc 164:H5327. https://doi.org/10.1149/2.0471708jes

59. Williams T, Shum R, Rappleye D (2021) Concentration Measurements In Molten Chloride Salts Using Electrochemical Methods. J Electrochem Soc 168:123510. https://doi.org/10.1149/1945-7111/ac436a

60. Bermejo MR, Gómez J, Medina J, et al (2006) The electrochemistry of gadolinium in the eutectic LiCl–KCl on W and Al electrodes. J Electroanal Chem 588:253–266. https://doi.org/10.1016/j.jelechem.2005.12.031

61. Lantelme F, Berghoute Y (1999) Electrochemical Studies of LaCl3 and GdCl3 Dissolved in Fused LiCl-KCl. J Electrochem Soc 146:4137–4144. https://doi.org/10.1149/1.1392604

62. Bermejo MR, Gómez J, Martínez AM, et al (2008) Electrochemistry of terbium in the eutectic LiCl–KCl. Electrochim Acta 53:5106–5112. https://doi.org/10.1016/j.electacta.2008.02.058

63. Caravaca C, de Córdoba G, Tomás MJ, Rosado M (2007) Electrochemical behaviour of gadolinium ion in molten LiCl–KCl eutectic. J Nucl Mater 360:25–31. https://doi.org/10.1016/j.jnucmat.2006.08.009

64. Deen WM (2012) Analysis of Transport Phenomena, 2nd ed. Oxford University Press, Inc., New York

65. Bird RB, Stewart WE, Lightfoot EN (2002) Transport Phenomena, 2nd ed. John Wiley & Sons, Inc., Hoboken, NJ

66. F. Bouarab A, Harvey J-P, Robelin C (2021) Viscosity models for ionic liquids and their mixtures. Physical Chemistry Chemical Physics 23:733–752. https://doi.org/10.1039/D0CP05787H

67. Zhao D, Yan L, Jiang T, et al (2023) On the viscosity of molten salts and molten salt mixtures and its temperature dependence. Journal of Energy Storage 61:106707. https://doi.org/10.1016/j.est.2023.106707

68. The American Ceramic Society and the National Institute of Standards and Technology (2023) Phase Equilibria Diagrams Online Database (NIST Standard Reference Database 31). In: Figure Numbers 16814 and 16114. https://www.nist.gov/srd/nist-standard-reference-database-31

69. Ackermann MN (1998) Why is Bismuth Subchloride Soluble in Acid? J Chem Educ 75:523. https://doi.org/10.1021/ed075p523

70. Diemente D (1997) Why is Bismuth Subchloride Soluble in Acid? J Chem Educ 74:398. https://doi.org/10.1021/ed074p398